

Comparison of two transmittance algorithms in the community radiative transfer model: Application to AVHRR

Yong Chen,^{1,2} Yong Han,^{3,4} and Fuzhong Weng^{3,4}

Received 31 July 2011; revised 30 January 2012; accepted 3 February 2012; published 23 March 2012.

[1] Two transmittance algorithms, Optical Depth in Absorber Space (ODAS) and newly developed Optical Depth in Pressure Space (ODPS), are currently available in the Community Radiative Transfer Model (CRTM) version 2. There are noticeable differences of simulated brightness temperature (BT) between the two algorithms for the Advanced Very High Resolution Radiometer's (AVHRR) three infrared channels. For channel 3, the BT difference is dependent on the zenith angle and is mainly caused by the plane-parallel atmospheric assumption used in ODAS. For channels 4 and 5, the differences arise from both zenith angle and gaseous absorption in the two algorithms. In the ODPS algorithm, a reduction in radiance due to chlorofluorocarbons (CFCs) absorption is partially offset by an increase due to a smaller local zenith angle at higher atmospheric levels. A further evaluation of the two transmittance algorithms was performed by comparing AVHRR simulated and observed BTs over ocean. Overall, ODPS is better than ODAS. The BT biases at channels 4 and 5 are dramatically improved in ODPS and very close to zero. At satellite nadir position, an inclusion of CFCs in ODPS reduces bias by 0.25, and 0.15 K for channels 4, and 5, respectively. However, the channel 3 bias shows a strong zenith angle dependence when it is larger than 40° in both the ODAS and ODPS simulations. This bias is due probably to the cloud contamination at larger zenith angles, and additional absorption in the atmosphere associated with other greenhouse gases such as carbon dioxide and water vapor.

Citation: Chen, Y., Y. Han, and F. Weng (2012), Comparison of two transmittance algorithms in the community radiative transfer model: Application to AVHRR, *J. Geophys. Res.*, 117, D06206, doi:10.1029/2011JD016656.

1. Introduction

[2] Community Radiative Transfer Model (CRTM) is a sensor-based fast radiative transfer model developed at the Joint Center for Satellite Data Assimilation (JCSDA) [Weng *et al.*, 2005; Han *et al.*, 2006; Chen *et al.*, 2008]. It can be used to simulate both radiances at the top of atmospheres and radiance gradients (or Jacobians) for satellites over various atmospheric and surface conditions, and is a key component in the data assimilation system of numerical weather prediction models. Currently, CRTM has been implemented in National Centers for Environmental Prediction (NCEP) Gridded Statistical Interpolation (GSI) for global data assimilation, the Global Modeling and Assimilation Office (GMAO) reanalysis system [Rienecker *et al.*,

2011], the Weather Research and Forecasting (WRF) model for radiance assimilation [Liu *et al.*, 2008], the Microwave Integrated Retrieval System (MIRS) for operational microwave products [Boukabara *et al.*, 2011], and the Advanced Clear-Sky Processor for Oceans (ACSPO) for the retrieval of sea surface temperature [Liang *et al.*, 2009].

[3] There are two transmittance algorithms available in CRTM version 2: ODAS (Optical Depth in Absorber Space) and ODPS (Optical Depth in Pressure Space); both algorithms are regression-based and differ primarily in vertical coordinates and the application of constraints to smooth vertical structures of the regression coefficients. The CRTM transmittance coefficients are derived by applying regression algorithms [McMillin *et al.*, 2006; Chen *et al.*, 2010] using the Line-by-Line (LBL) transmittances convolved with the instrument spectral response functions (SRFs) as predictands, and atmospheric state variables as predictors. With an increasing demand of a better accuracy in the CRTM for weather and climate applications, the ODPS algorithm is developed by including additional gaseous absorbers such as chlorofluorocarbons [Chen *et al.*, 2010], which were not considered in the ODAS algorithm in the past.

[4] As long-lived compounds in the atmosphere, chlorofluorocarbons (CFCs), consisting primarily of CCl₃F (CFC-11), CCl₂F₂ (CFC-12), and CCl₂FCClF₂ (CFC-113), are a

¹Cooperative Institute for Research in the Atmosphere, Colorado State University, Fort Collins, Colorado, USA.

²Joint Center for Satellite Data Assimilation, Camp Springs, Maryland, USA.

³Center for Satellite Applications and Research, National Environmental Satellite, Data, and Information Service, NOAA, Camp Springs, Maryland, USA.

⁴Also at Joint Center for Satellite Data Assimilation, Camp Springs, Maryland, USA.

Table 1. Summary of CFCs and CCl₄ Represented by IR Cross-Section Data in HITRAN [Rothman *et al.* 2005] and Concentration Used in This Study

Molecule	Common Name	Temperature Range (K)	Pressure Range (torr)	Number of T, P Sets	Spectral Coverage (cm ⁻¹)	Concentration (ppt)
CCl ₃ F	CFC-11	190–296	8–760	55	810–880	246
CCl ₂ F ₂	CFC-12	190–296	8–760	55	1050–1120	540
		190–296	8–760	52	850–950	
		190–296	8–760	52	1050–1200	
CCl ₂ FCClF ₂	CFC-113	203–293	0	6	780–995	74
		203–293	0	6	1005–1232	
CCl ₄	Carbon tetrachloride	208–297	8–760	32	750–812	90

main source for the depletion of stratospheric ozone [Molina and Rowland, 1974; World Meteorological Organization (WMO), 1988; Elkins *et al.*, 1993], and have a significant absorption in Advanced Very High Resolution Radiometer (AVHRR) channels 4 and 5 [Saunders and Edwards, 1989; Christidis *et al.*, 1997; Coheur *et al.*, 2003; Dufour *et al.*, 2005]. The AVHRR is onboard a series of NOAA and Meteorological and Operation (MetOp) satellites. It includes three infrared (IR) window channels: 3B (3.7 μm , the range of spectral response $\sim 2400\text{--}3000\text{ cm}^{-1}$), 4 (11 μm , $\sim 850\text{--}1000\text{ cm}^{-1}$) and 5 (12 μm , $\sim 790\text{--}890\text{ cm}^{-1}$). Since 1978, the AVHRR data have been extensively used for deriving the sea surface temperature (SST) and other environmental parameters [McClain *et al.*, 1985; Ignatov *et al.*, 2004; Reynolds *et al.*, 2007]. To accurately generate the AVHRR top-of-atmosphere (TOA) radiance over oceans, and to derive SST and aerosol products, the important absorption of CFCs must be considered in the radiative transfer process. In the ODPS algorithm, the three most abundant CFCs (CFC-11, CFC-12, and CFC-113) and carbon tetrachloride (CCl₄) are included, and a summary of the four molecules represented by IR cross-section data in High Resolution in Transmission (HITRAN) [Rothman *et al.*, 2005] is given in Table 1.

[5] An accurate representation of the global sea surface temperature is important for many marine applications, numerical weather prediction (NWP), and for monitoring the global climate. To explore improvements in sea surface temperature retrieval from AVHRR instruments on board the NOAA and MetOp satellites, an accurate and globally representative fast radiative transfer model such as CRTM is needed [Liang *et al.*, 2009]. In this paper, the two transmittance algorithms in the CRTM version 2 are specifically compared for simulations of brightness temperatures at AVHRR infrared channels. The paper is organized as follows. A description of these two algorithms is given in section 2. Section 3 discusses the inclusion of CFCs in the transmittance model and the impacts from these new gaseous absorptions on brightness temperature simulations. Evaluation of these two algorithms using observations from AVHRR on the MetOp-A is presented in section 4. The possible reasons are discussed in Section 5 to explain the discrepancy between model simulations and observations. Section 6 highlights some major conclusions.

2. Model Description

[6] Recently, the CRTM version 2 is released to user communities for various applications. In this version, there

are two transmittance algorithms available for use: ODAS, which is an improved version of Optical Path TRANsmittance (OPTRAN) algorithm [McMillin *et al.*, 2006]; and ODPS [Chen *et al.*, 2010], which is similar to the Radiative Transfer for the Television and infrared observation satellite Operational Vertical Sounder (RTTOV)-type of transmittance algorithm [Saunders *et al.*, 1999]. The algorithms can be selected by user via different transmittance coefficient data files used to initialize the CRTM. To generate the coefficients in the regression algorithms, a set of diversified profiles of atmosphere states (such as temperature, water vapor, ozone, *et al.*) is used to prepare the training set of predictands and predictors. The profiles are chosen to represent the range of variations in temperature and absorber amount found in the real atmosphere such as the European Centre for Medium-Range Weather Forecasts (ECMWF) 83 profiles [Chevallier *et al.*, 2006], and the University of Maryland at Baltimore County (UMBC) 48 profiles [Strow *et al.*, 2003]. The predictands are layer LBL transmittances convolved SRFs and the predictors are layer atmospheric variables. Chen *et al.* [2010] provides a detail comparison of the ODAS and ODPS regression algorithms. Both ODAS and ODPS regression coefficients were trained with the same version (v11.3) of the Line-by-line Radiative Transfer Model (LBLRTM) [Clough *et al.*, 2005] in this study. The fitting errors in terms of mean difference and root mean square (RMS) difference for both algorithms are very small. The fitting errors for AVHRR on MetOp-A three infrared channels related to the LBLRTM reference (including the first 7 molecules H₂O, CO₂, O₃, N₂O, CO, CH₄ and O₂, and only H₂O and O₃ allowed to vary) using ECMWF 83 atmospheric profile set are summarized in Table 2. Based on Table 2, both algorithms are very accurate compared to the results from LBLRTM. Although ODAS has similar performance compared to ODPS for broadband IR channels, it is difficult to be extended to include more variable gases due to technical related reasons instead of fundamental physical

Table 2. Summary of the Fitting Errors for AVHRR on MetOp-A Three Infrared Channels Related to the LBLRTM Reference Using ECMWF 83 Atmospheric Profile Set

Algorithm	Mean Difference From Reference (K)			RMS (K)		
	Channel 3	Channel 4	Channel 5	Channel 3	Channel 4	Channel 5
ODAS	−0.0005	0.0063	0.0042	0.0132	0.0589	0.0660
ODPS	0.0078	0.0006	0.0029	0.0264	0.0145	0.0208

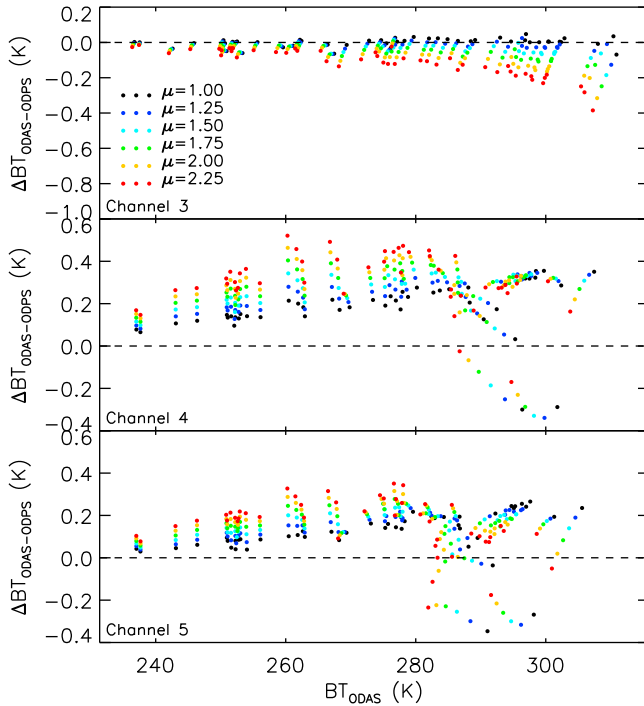


Figure 1. Brightness temperature difference between ODAS and ODPS for MetOp-A AVHRR3 in CRTM with same surface zenith angle for UMBC 48 profiles and for 6 zenith angles.

reason. To include three or more variables gases, a correction factor is needed to account for the difference between the total transmittance and the product of the individual gas transmittances in ODAS [Han *et al.* 2003]. When an additional variable gas is included, predictors related to this gas such as absorber amount, its different polynomial orders, and its product with pressure are needed to be added to the predictor pool for predicting the correction factor. Furthermore, the correction factor has no physical constraints and is very difficult to represent and model using polynomial basis functions. ODAS includes the first 7 molecules H_2O , CO_2 , O_3 , N_2O , CO , CH_4 and O_2 in LBLRTM, whereas ODPS adds 10 more trace gases (NO , SO_2 , NO_2 , HNO_3 , OCS , N_2 , CCl_4 , CCl_3F (CFC-11), CCl_2F_2 (CFC-12), and CCl_2FCClF_2 (CFC-113)). In the ODAS algorithm, the concentrations of H_2O and O_3 are variables for all IR sensors. In the ODPS algorithm, the concentrations of H_2O , CO_2 and O_3 are variables for broadband satellite IR channels. For hyper-spectral infrared sounders such as Atmospheric Infrared Radiance Sounder (AIRS), the Infrared Atmospheric Sounding Interferometer (IASI), and Cross-track Infrared Sounder (CrIS), the ODPS algorithm can have up to six user input variable absorbers: H_2O , CO_2 , O_3 , N_2O , CO and CH_4 . For other gases, referred as fixed gases, included in the LBLRTM computations, their mixing ratios are held constant, assuming that their spatial and temporal concentration variations do not contribute significantly to the observed radiances. The profiles of CCl_4 , CFC-11, CFC-12, and CFC-113 were scaled to reflect present-day concentrations based on data from Scripps Institution of Oceanography (SIO) 2005 calibration scale: CFC-11 (246 ppt), CFC-12 (540 ppt), CCl_4 (90 ppt), and CFC-113 (74 ppt).

[7] Unlike ODAS, the ODPS algorithm also considers the Earth curvature effect by varying the local zenith angle with height. The angular dependence of the optical depth is expressed as the vertical optical depth divided by the secant of the local zenith angle. Due to the Earth curvature, the satellite view angle should be converted into a local zenith angle which decreases with altitude. However, this was ignored in the ODAS algorithm where a constant local zenith angle is used throughout the atmosphere (i.e., plane-parallel assumption). In the LBLRTM calculation, the output layer transmittances include the effects of the curvature of the Earth with the local zenith angles at seven different angles (namely the angle for which the secant has equally spaced values from 1 to 2.25 plus an additional value of 3.0) at TOA. When using a regression method to train the ODAS transmittance coefficients with LBLRTM transmittances, we assumed that the local zenith angle is constant with height and used the TOA zenith angle in LBLRTM. However, the ODPS transmittances use the same local zenith angles as those in LBLRTM which vary with height. For the same TOA zenith angle, ODPS has a larger local zenith angle than ODAS below the TOA height since ODPS follows the LBLRTM zenith angle profiles. The local zenith angle at the bottom of each layer can be computed according to Snell's law:

$$\sin(\theta_i) = \sin(\theta_{sat}) \frac{R_{earth} + H_{sat}}{R_{earth} + H_i} \cdot \frac{n_{top}}{n_i} \quad (1)$$

where θ_{sat} is the satellite scan angle, R_{earth} is the radius of the Earth for a given latitude, H_{sat} is the altitude of the satellite, H_i is the height of the bottom of layer i , n_i is the index of refraction of air through layer i and n_{top} is the index of refraction of air [Ciddor, 1996] at TOA (in CRTM, the TOA is set to 0.005 hPa).

[8] In order to compare the performance of these two transmittance algorithms in CRTM, we applied them to the AVHRR infrared window channels at nighttime over ocean. Neglecting cosmic radiation and atmospheric scattering for the AVHRR IR channels, the clear-sky IR channel radiance at TOA can be physically expressed as:

$$R_i(\theta) = \varepsilon_i(\theta_s) \cdot B_i(T_s) \cdot \tau_i^\uparrow(\theta_s) + (1 - \varepsilon_i(\theta_s)) \cdot L_i^\downarrow(\theta) \cdot \tau_i^\uparrow(\theta_s) + L_i^\uparrow(\theta) \quad (2)$$

where i is the sensor channel number, θ_s is the local zenith angle at surface, θ is the local zenith angle (constant in ODAS, but varying with height in ODPS), T_s is the sea surface temperature, $B(T_s)$ is the Planck radiance, ε is the surface emissivity, τ^\uparrow is the upwelling atmospheric total transmittance, and L^\downarrow and L^\uparrow are the atmospheric upwelling and downwelling radiances, respectively. The three terms in the right hand side of equation (2) are the contributions from surface emission, surface reflection of atmospheric downwelling radiance, and atmospheric upwelling radiance, respectively.

3. CRTM Simulations and Comparisons

[9] In this section, we focus on the two transmittance algorithms' performance in CRTM, and for simplicity we set the surface emissivity to one. Figure 1 shows the CRTM

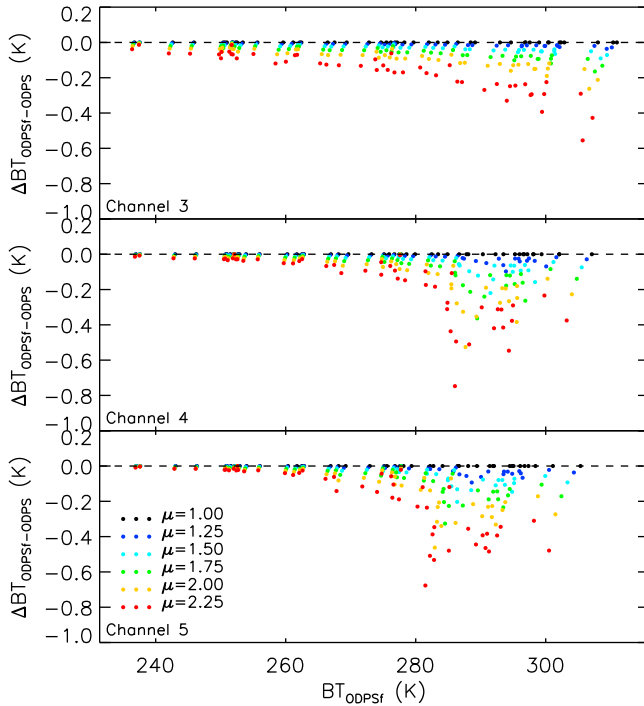


Figure 2. Path angle impact for ODPS. Surface zenith angle for ODPSf is TOA zenith angle in LBLRTM and fixed at each level as ODAS, while ODPS is using same surface zenith angle but path angle changing with profile height.

simulated brightness temperature difference (ΔBT) between ODAS and ODPS for AVHRR on MetOp-A satellite. These differences are calculated by using UMBC 48 diverse atmospheric profiles at different surface zenith angles of 0.0° , 36.87° , 48.19° , 55.15° , 60.0° , and 63.61° (the secant of zenith angles $\mu = 1/\cos(\theta)$ are 1, 1.25, 1.50, 1.75, 2.00, and 2.25) with fixed surface emissivity equal to 1. For channel 3, the ΔBT s are near zero at nadir (surface zenith angle at 0.0°), and negative at other zenith angles. Their difference increases with the zenith angle. However, the ΔBT s of channels 4 and 5 show different pattern from these of channel 3 with most positive values. At nadir the ΔBT s are around 0.2 K and 0.1 K for channel 4 and channel 5, respectively.

[10] The BT differences between ODAS and ODPS can be mainly explained by the two factors as highlighted in the previous section: local zenith angle correction and absorber gases included. In the CRTM simulation, the surface zenith angle instead of TOA zenith angle is a mandatory input. For the same surface zenith angle, the ODPS results in a larger brightness temperature due to the smaller TOA zenith angle at higher levels (with smaller column of absorber gases) than in ODAS. In order to illustrate the impact of path angle on BT computation, we compared the CRTM simulated BT differences between ODPS with a fixed TOA zenith angle in all levels (referred to ODPSf) and ODPS using LBLRTM zenith angle profiles. The results are shown in Figure 2 for UMBC 48 profiles and at six TOA zenith angles. All three AVHRR channels show the same patterns. The ΔBT s are exactly zero at nadir, and negatively increase as the zenith angle increases. These results suggest that the BT differences between ODAS and ODPS in CRTM are mainly due

to zenith angle differences for channel 3, while for channel 4 and channel 5, the ΔBT s in Figure 1 might be due to the difference of additional absorber gases included in the training process. Figure 3 shows the BT difference between CRTM ODAS simulations (without CFCs) versus LBLRTM v11.3 computation with the previous mentioned 10 trace gases for UMBC 48 profiles at 6 zenith angles. The BT difference shows that channel 3 does not sensitive to CFCs. However, sensitivity test found that channels 4 and 5 are more sensitive to CFCs than the other trace gases (no shown here). By considering the CFCs absorption in the LBLRTM, the BTs are reduced 0.33 K and 0.21 K for channel 4 and channel 5, respectively.

[11] Based on these simulations and comparisons, we now can largely explain the brightness temperature difference for the three AVHRR IR channels between the ODAS algorithm and the ODPS algorithm in CRTM with the same surface zenith angle: (1) Channel 3 zenith angle dependence difference is mainly caused by plane-parallel atmospheric assumption in ODAS. ODPS should give more accurate result than ODAS compared to LBLRTM if both algorithms use same surface zenith angle. (2) Channels 4 and 5 BT differences come from both path angle and absorber gases difference for these two algorithms. In the ODPS algorithm, reducing radiance due to CFCs absorption is partially offset the increasing radiance due to smaller path zenith angles at higher atmospheric levels.

4. Evaluation With Observations

[12] Evaluation of the two transmittance algorithms was performed by comparing the CRTM simulated brightness

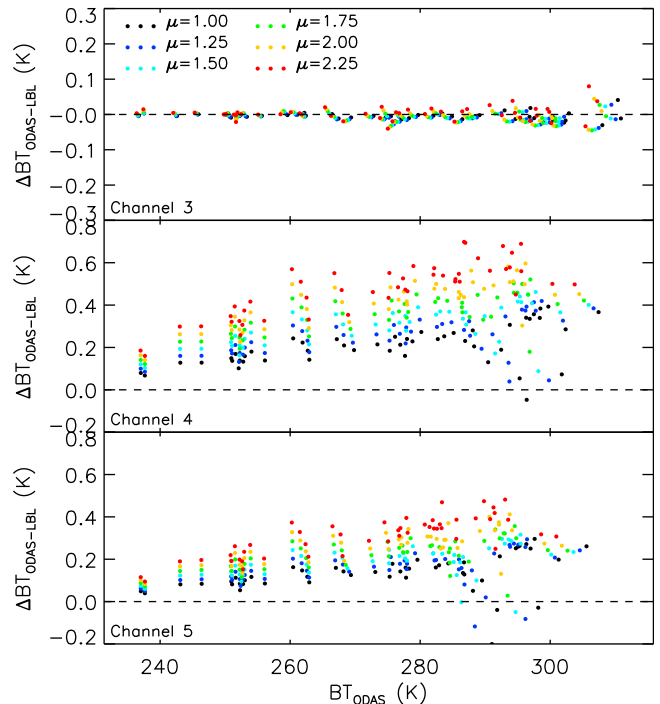


Figure 3. Brightness temperature differences between CRTM ODAS simulations and LBLRTM v11.3 with CFCs for UMBC 48 profiles.

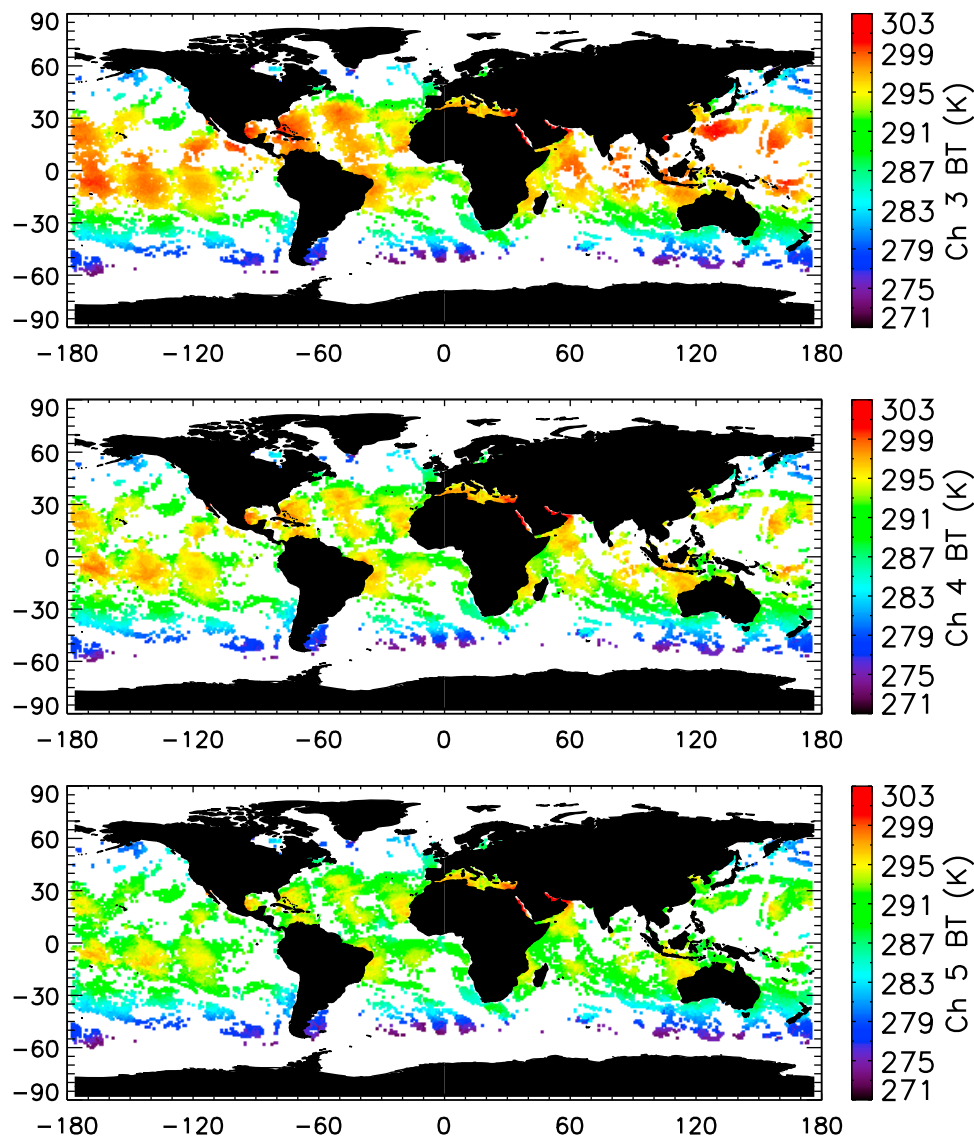


Figure 4. Observation brightness temperature for AVHRR channels 3 to 5 on August 1, 2009.

temperatures with the MetOp-A AVHRR observations. To best simulate the infrared window channel, the surface emissivity chosen must be accurate. In this study, we compare the simulations from two ocean emissivity models. The first is the *Wu and Smith* [1997] model (referred to as Wu-Smith model), and the second is the *Nalli et al.* [2008a] model (referred to as Nalli model). The two models are implemented in CRTM version 2, and can be selectable by user via the emissivity data file. The main difference between the two models is that Nalli model introduced an “effective emissivity” that accounts for the diffuse component of the quasi-specular sea surface for large atmospheric path angle greater than 40° .

[13] For an Infrared channel, the clear sky TOA brightness temperature simulation from CRTM has two primary components: the surface emission and reflection model, the atmospheric transmittance and emission model. In order to evaluate the accuracy of the transmittance algorithms and the surface emissivity models in contributing to the modeled

TOA satellite simulations, the CRTM was run with three settings respectively: ODAS with Wu-Smith model, ODPS with Wu-Smith model and ODPS with Nalli model. One day data of AVHRR (resolution ~ 4 km for Global Area Coverage) on MetOp-A (total 14 orbit data) on August 1, 2009 was selected for comparison with CRTM model simulations in three window channels. The AVHRR data is downloaded from NOAA’s Comprehensive Large Array-data Stewardship System (<http://www.class.ncdc.noaa.gov>). The data itself includes cloud mask derived from cloud detection scheme in the extended Clouds from AVHRR (CLAVR-x) system [Heidinger, 2004].

[14] Atmospheric and surface analysis fields from the European Centre for Medium-Range Weather Forecasts (ECMWF) were used as inputs to CRTM. However, over ocean the ECMWF sea surface temperatures were replaced by OSTIA (operational sea surface temperature and sea ice analysis system) global sea surface temperature. The OSTIA data is daily, global coverage $1/20^\circ$ (~ 6 km) high resolution

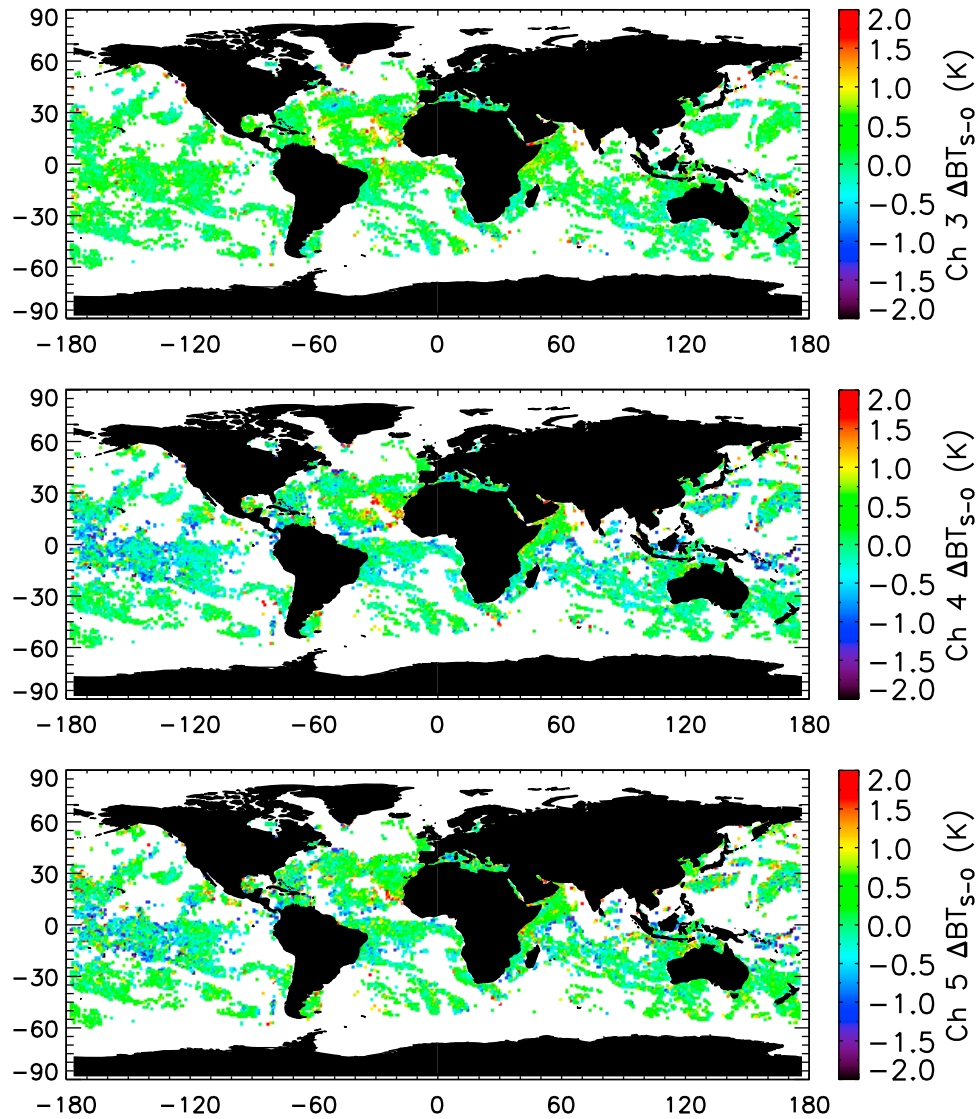


Figure 5. Brightness temperature differences between CRTM ODPS simulations (with Wu-Smith model) and observations.

data set from the United Kingdom Met Office [Stark *et al.*, 2007]. The ECMWF atmospheric profiles (pressure, temperature, water vapor, and ozone) had 91 vertical layers on a global grid of 0.25° spatial resolution. For a given satellite pixel, the spatial and temporal interpolation from the analysis fields is performed as follows: First, the four analysis grid points surrounding the satellite pixel were bilinearly interpolated to the location of satellite pixel location, then a linear temporal interpolation in time was performed using two analysis fields that bound the AVHRR observational time.

[15] With the inputs of collocated atmospheric and surface analysis fields, CRTM was used to simulate TOA brightness temperature at three AVHRR channels for three cases: the ODAS transmittance algorithm with Wu-Smith emissivity model (ODAS_W), the ODPS transmittance algorithm with Wu-Smith emissivity model (ODPS_W), and ODPS transmittance algorithm with Nalli model (ODPS_N), and each of

them was compared to AVHRR observed BT for cloud-free, ocean pixels at nighttime. The cloud-free pixels are determined when the AVHRR cloud mask flag equal to zero and nine-neighboring-points standard deviation of channel 4 is less than 0.3 K. Nighttime pixels are defined when the solar zenith angle is greater than 118° [Cao *et al.*, 2001]. Figure 4 shows the global distribution of clear sky BT for AVHRR channels 3 to 5 on August 1, 2009 over ocean at nighttime. The corresponding brightness temperature differences between CRTM ODPS simulation with Wu-Smith's sea surface emissivity model, ODPS_W, and observation (S-O) are shown in Figure 5. For all the three channels the simulated BTs show a very good agreement with observations, with maximum absolute differences less than 2.0 K, and most of them are around zero. The simulated ΔBT s from the two transmittance algorithms ODPS and ODAS with Wu-Smith emissivity model are shown in Figure 6. The most prominent feature in Figure 6 is the negative ΔBT s increase

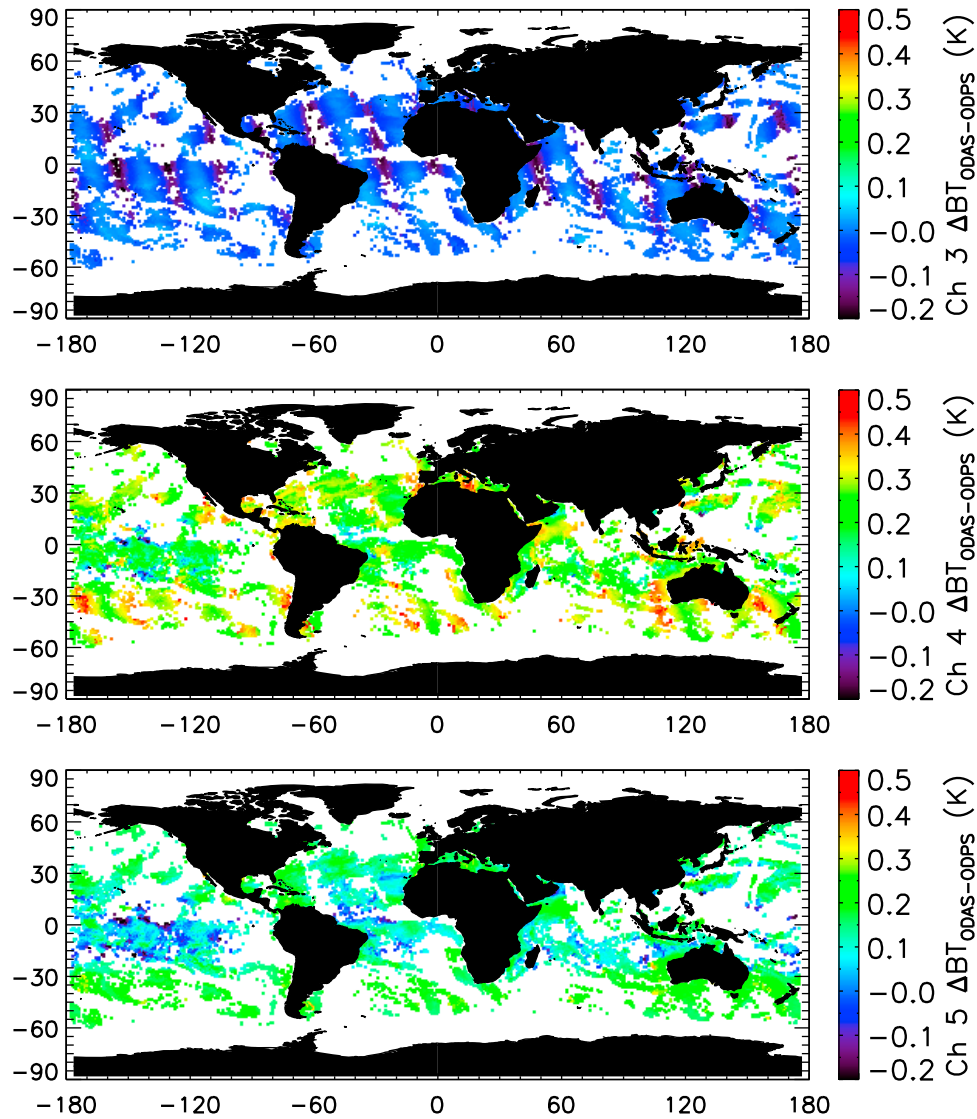


Figure 6. Brightness temperature difference between CRTM ODAS and ODPS with Wu-Smith model.

toward the edge of the scan for channel 3. However, the ΔBT s for channels 4 and 5 show more uniform global distribution, regardless of the satellite zenith angle. The mean ΔBT for channel 4 is ~ 0.25 K and is greater than channel 5 (~ 0.15 K). Figure 7 shows the histograms of the simulations minus observations for AVHRR channels 3 to 5 for three cases, ODPS_W, ODAS_W, and ODPS_N. For channel 3, the mean biases for the three cases are as small as 0.1 K, although ODAS_W shows the best results and ODPS_N show larger positive bias. For channel 4, the results from the ODPS algorithm are much better than those from ODAS. The biases are very small around -0.05 K for ODPS_W, and -0.02 K for ODPS_N, but the bias from ODAS_W is 0.2 K. The Channel 5 is similar to channel 4: the bias in ODPS_W is the smallest, and ODAS_W is the largest. The brightness temperature bias and standard deviation as a function of satellite zenith angle are shown in Figure 8. The channel 3 bias shows strong zenith angle dependence when zenith angle greater than 40° regardless of the transmittance algorithms and sea surface models used. For the same sea

surface model (Wu-Smith model), ODPS is more dependent on zenith angle than ODAS for channel 3. The Nalli model increases the zenith angle dependence for all the three channels. Channel 4 and channel 5 biases are dramatically smaller in ODPS than ODAS. The including of CFCs in the ODPS algorithm contributes to the biases reduction of ~ 0.25 K for channel 4 and ~ 0.15 K for channel 5 at nadir.

5. Discussion

[16] It is understandable that the Nalli model have larger simulated BT than the Wu-Smith model at satellite zenith angle greater than 40° since Nalli model considers the reflected radiance at larger angles for the downwelling diffuse radiance, where a specular reflection is assumed when Wu-Smith model is used to compute the emissivity. Theoretically, the Nalli's model is more accurate than the Wu-Smith's model, and has been validated against surface-based Marine Atmospheric Emitted Radiance Interferometer (M-AERI) data [Nalli *et al.*, 2008b]. It seems to contradict with the results shown in Figure 8, which shows that Nalli

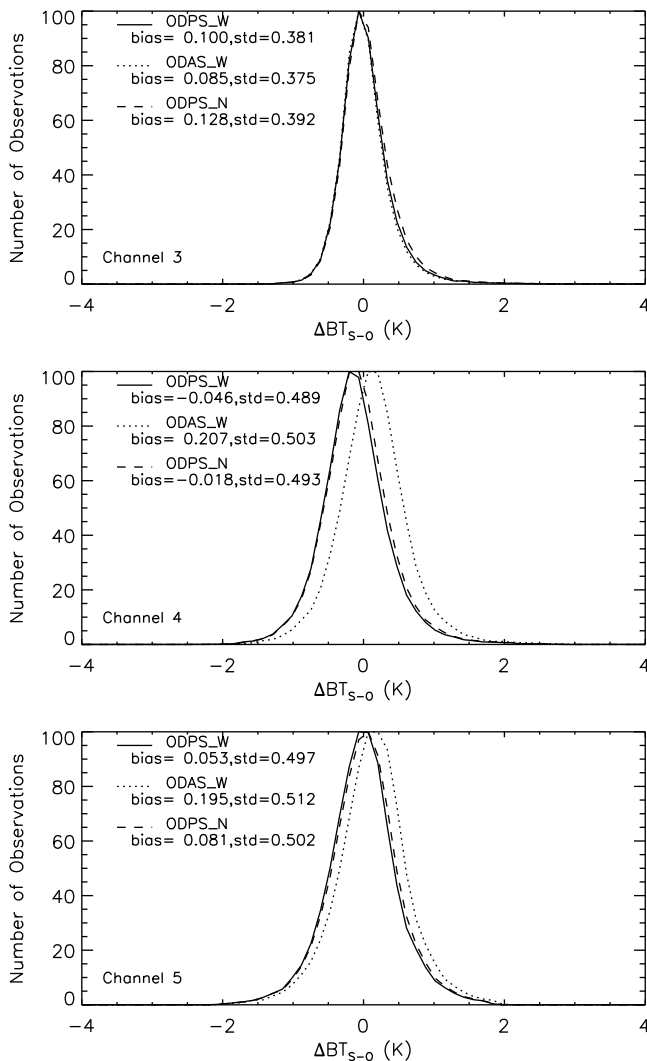


Figure 7. Histogram of simulation minus observation for AVHRR channels 3 to 5.

model has larger biases compared to Wu-Smith model, especially for channel 3. It may indicate: there may have some errors in the forward model itself; the state parameters used in the forward model may not be accurate enough; there are residual clouds remaining in “clear-sky” radiances leading to suppressed observation with greater angles thus a concave-up simulation minus observation (S-O) variation with zenith angle; there are missing aerosols in the simulations. In the following, we present several possible reasons which may explain the discrepancy.

5.1. Impact of LBLRTM Model Improvements

[17] The coefficients in CRTM transmittance algorithms are trained with LBLRTM v11.3, which was released in November 2007. The more recent LBLRTM release version is v11.7, which includes important modifications for MTCKD v2.5 CO₂ continuum from 2000 to 3000 cm⁻¹ and water vapor self continuum from 2000 to 3200 cm⁻¹ based on analysis of IASI, AIRS, and AERI measurements in these regions. The AVHRR channel 3 spectral response is located within this wavelength region. Figure 9 shows the impact of the LBLRTM model improvements from v11.3 to v11.7 on

AVHRR channel 3 brightness temperatures based on the diverse ECMWF 83 atmospheric profiles as a function of zenith angle. The mean difference at nadir is ~ 0.1 K, increases with the zenith angle, and can reach to 0.3 K at zenith angle of 70°. The improvement of LBLRTM would reduce about 0.1 K difference for larger zenith angles at channel 3, which can’t fully explain the concave-up S-O feature.

5.2. Impact of Residual Cloud

[18] The warm S-O bias at the larger zenith angle may be in part due to a cold bias in the AVHRR observation BTs originating from the cloud contamination in the FOV. To test the impact of the cloud contamination on BT, we assume a very lower water cloud over ocean, with particle size as 7.5 μm , and water content as 0.1 kg/m². The brightness temperature differences between clear sky and cloudy sky as a function of satellite zenith angle and cloud fraction are shown in Figure 10. The ΔBT from channel 3 is more sensitive to this water cloud than channels 4 and channel 5. The maximum ΔBT is 5.39 K for channel 3, and only 0.58 K for channel 4 and 0.38 K for channel 5. For a fixed cloud fraction, the ΔBT s from channels 4 and 5 decrease with the zenith angle increasing. However, the ΔBT s from channel 3 increase with the zenith angle. For a 0.1 cloud fraction, the ΔBT from channel 3 can be large as ~ 0.45 K, whereas the ΔBT s from channel 4 and channel 5 are less than 0.05 K. For a larger zenith angle, the effective cloud fraction increases [Taylor and Ellingson, 2008] compared to nadir. The residual clouds thus may contribute to a concave-up signal in S-O bias.

5.3. Impact of Aerosol

[19] To estimate the aerosol effect on the global S-O bias, the aerosol fields should be specified from an established global model, e.g., the Goddard Chemistry Aerosol Radiation and Transport Model (GOCART) [Chin et al., 2000]. GOCART model simulates major tropospheric aerosol components, including sulfate, dust, black carbon, organic carbon, and sea-salt aerosols. The same GOCART aerosol physics have been implemented into CRTM. We obtained August 1, 2009 (4 times 03Z, 09Z, 15Z, 21Z) GOCART model output, and performed the spatial and temporal interpolation from the analysis fields to the AVHRR observation locations and times to get the aerosol profiles. Figure 11 shows the mean and standard deviation of the aerosol impact on AVHRR three channels brightness temperature over ocean as a function of satellite zenith angle for ODPS algorithm under clear sky without aerosol and with aerosol. Note that the statistics is only made for dust-free oceanic conditions, and BT differences greater than 0.5 K are screened out. Overall, the aerosol impact on the TOA BTs is ~ 0.02 K for the AVHRR three channels, and only for channel 3 it increases with the satellite zenith angle. The impact of aerosol on the channel 3 radiances is the same order of channels 4 and 5 may indicate that the aerosol module in CRTM needs to be improved, which is well beyond the scope of this work.

5.4. Impact of CFC Concentration

[20] The profiles of CCl₄, CFC-11, CFC-12, and CFC-113 in this study were scaled to reflect present-day

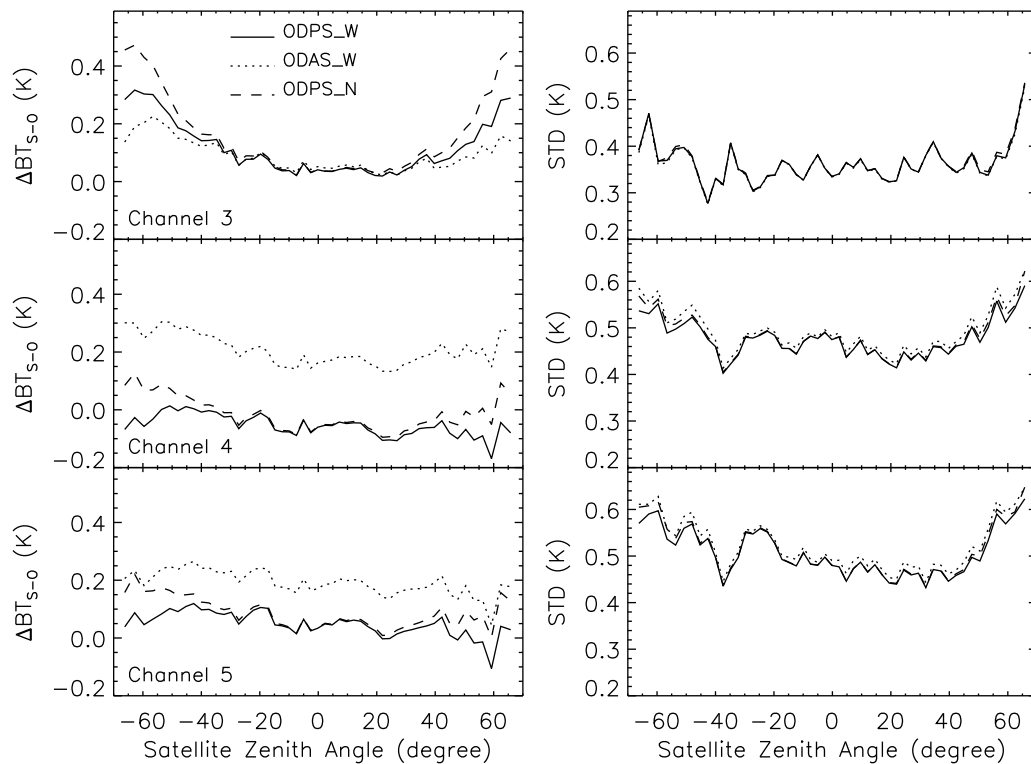


Figure 8. Brightness temperature (left) bias and (right) standard deviation as a function of satellite zenith angle for CRTM simulation compared to observation.

concentrations as given in Table 1. However, the concentrations of CFCs and CCl_4 continue to decrease due to control of the international regulations, and also demonstrate non-negligible difference between Northern and Southern Hemisphere [Walker *et al.*, 2000]. For example, mixing ratios of CFC-12, which account for about one-third of the current atmospheric chlorine loading, have been constant within 1% (5 ppt) since 2000, and some in situ and Northern Hemisphere column measurements show that peak values were attained in 2003. CFC-11 mixing ratios are decreasing at approximately 1.9 ppt/yr and CFC-113 mixing ratios are decreasing by approximately 0.8 ppt/yr [WMO, 2007]. In order to understand the impact of these concentration changes, we have tested the sensitivity of the TOA brightness temperature to CFCs and CCl_4 change in LBLRTM. The results are shown in Figure 12. With CFCs concentration change $\pm 10\%$, there is no impact on AVHRR channel 3. The impact on channel 4 is the largest with average difference BTs are 0.014 K, 0.030 K for $\mu = 1.0$ and $\mu = 2.25$, respectively for the ECMWF 83 profiles. For channel 5, the average difference BTs are 0.010 K, and 0.022 K for $\mu = 1.0$ and $\mu = 2.25$, respectively. We should point out that although 10% changes in CFCs cause very small change in BTs, BTs can be reduced by 0.33 K and 0.21 K for channel 4 and channel 5, respectively if we don't consider CFCs absorptions.

6. Summary and Conclusions

[21] In this study, two transmittance algorithms, ODAS and ODPS, have been compared and evaluated for the AVHRR on MetOp-A three infrared channels brightness

temperatures under the CRTM version 2. For the same input state variables, there are noticeable simulated BT differences between ODAS and ODPS algorithms. After a careful examination of the two algorithms differences, we found that Channel 3 zenith angle dependence difference is mainly caused by plane-parallel atmospheric assumption in ODAS, and this Earth curvature effect was taken into account in ODPS; Channels 4 and 5 BT differences come from both zenith angle and absorber gases difference for these two algorithms. In the training of ODPS algorithm, 10 more trace gases (especially CFCs) have been added in LBLRTM v11.3

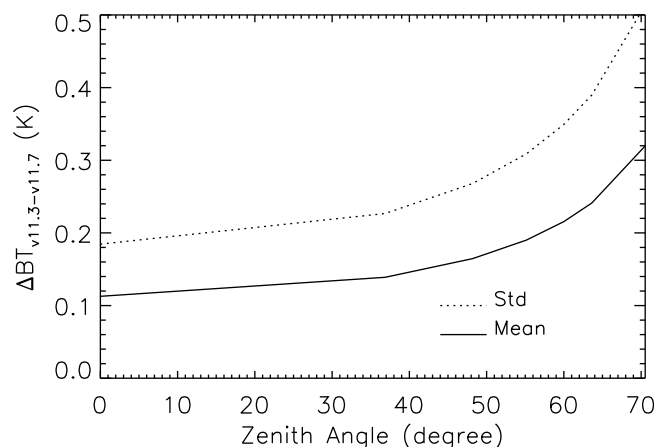


Figure 9. The mean and standard deviation of the LBLRTM version change impact on AVHRR channel 3 brightness temperature with the ECMWF 83 profile.

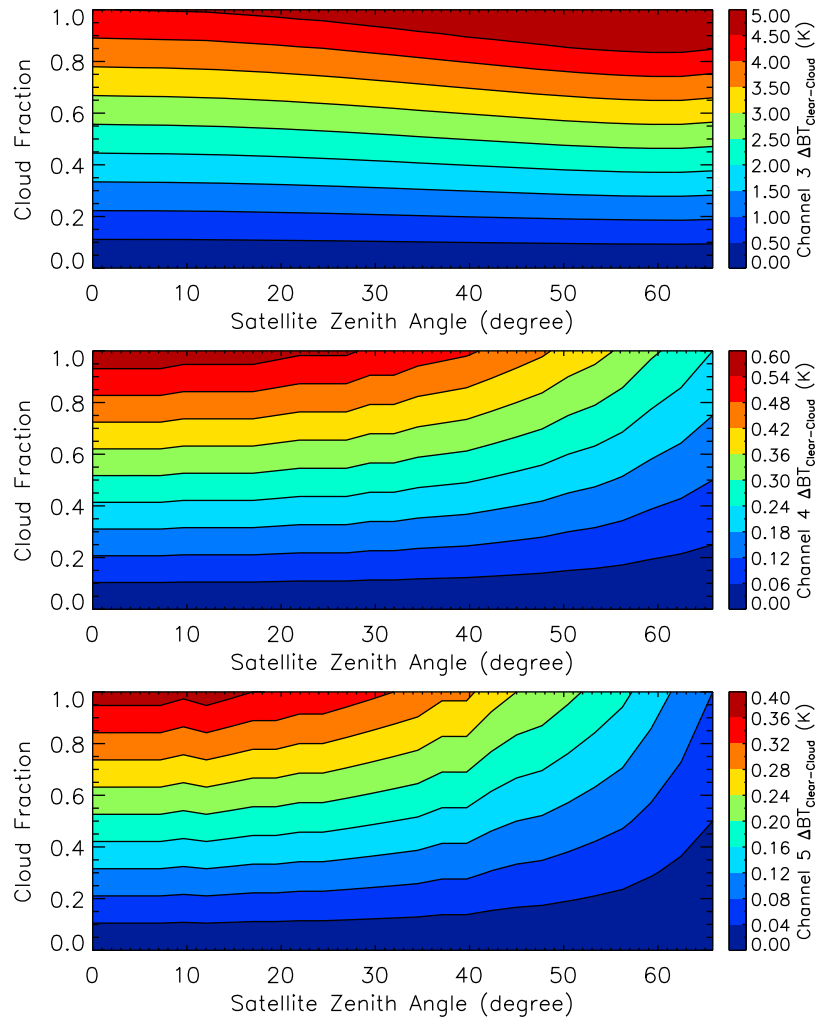


Figure 10. The brightness temperature differences between clear sky and cloudy sky (very lower cloud) as a function of satellite zenith angle and cloud fraction.

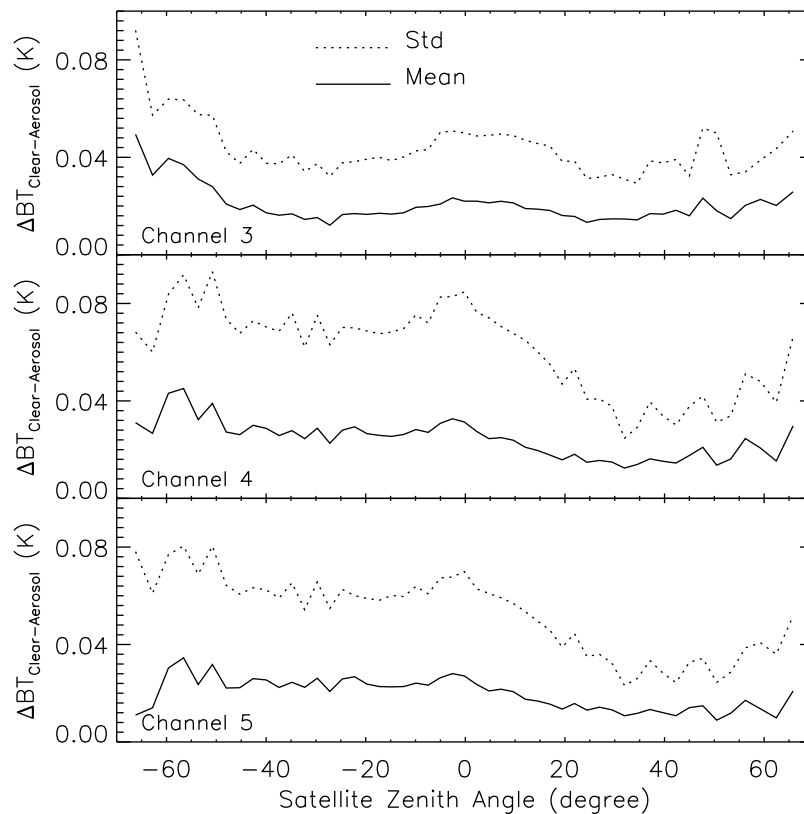


Figure 11. The mean and standard deviation of the aerosol impact on AVHRR three channels brightness temperature as a function of satellite zenith angle.

computations. The BTs can be reduced by 0.33 K and 0.21 K for channel 4 and channel 5 due to CFCs absorption, respectively.

[22] These two transmittance algorithms, with two ocean emissivity models: Wu-Smith model and Nalli model, in CRTM v2 have been evaluated with AVHRR observations at night on August 1 2009. We found that the ODPS algorithm offers substantial improvement for AVHRR channel 4 and channel 5. The inclusion of CFCs in the ODPS algorithm contributes to the biases reduction of ~ 0.25 K for channel 4 and ~ 0.15 K for channel 5 at nadir. When zenith angle is greater than 40° , channel 3 simulation-minus-observation bias shows strong zenith angle dependence regardless of the transmittance algorithms and sea surface models used. For the same sea surface model (Wu-Smith model), the bias from the ODPS algorithm is more dependent on zenith angle than from the ODAS algorithm for channel 3. The Nalli model increases the zenith angle dependence for all the three channels.

[23] It is also found that improvement of CO_2 continuum from 2000 to 3000 cm^{-1} and water vapor self continuum from 2000 to 3200 cm^{-1} in LBLRTM v11.7 from v11.3 would reduce about 0.1 K difference for larger zenith angles at channel 3; The cloud (very low level water cloud) contamination in the FOV at larger zenith angles in AVHRR observation may contribute to the concave-up signal in S-O bias; The presence of aerosol in the atmosphere may also have contribution although the impact is smaller than previous two reasons in our simulation.

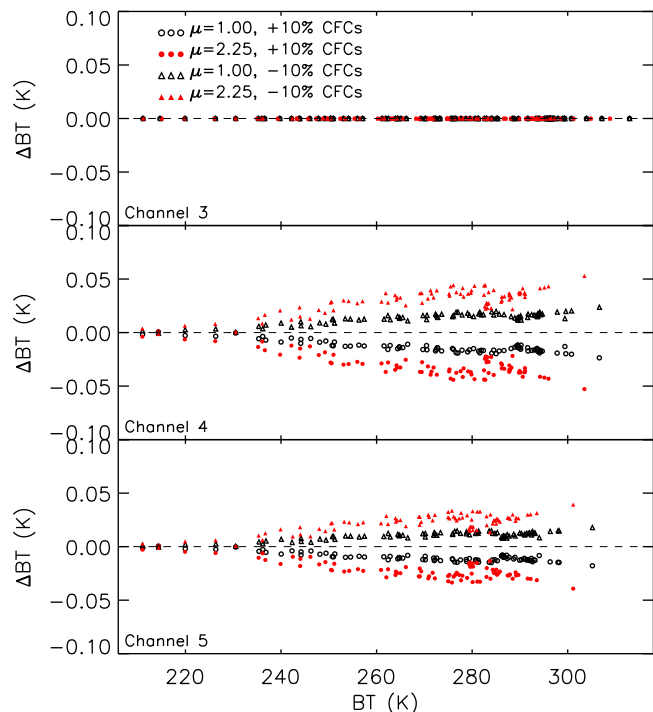


Figure 12. CFCs concentration changes impact on AVHRR three channels brightness temperature with the ECMWF 83 profiles.

[24] **Acknowledgments.** The authors thank Xiaozhen Xiong and Xu Li for their critical review and judicious comments. Thanks are also extended to Quanhua Liu for his help with aerosol impact simulations, Paul van Delst for the CRTM software integration, and three anonymous reviewers for their very useful suggestions to improve our paper. This research was supported by Chinese Ministry of Science and Technology under 973 project 2010CB951600 and the Joint Center for Satellite Data Assimilation program. The contents of this paper are solely the opinions of the authors and do not constitute a statement of policy, decision, or position on behalf of NOAA or the U. S. Government.

References

- Boukabara, S. A., et al. (2011), MiRS: An all-weather 1DVAR satellite data assimilation and retrieval system, *IEEE Trans. Geosci. Remote Sens.*, **49**, 3249–3272, doi:10.1109/TGRS.2011.2158438.
- Cao, C., M. Weinreb, and J. Sullivan (2001), Solar contamination effects on the infrared channels of the advanced very high resolution radiometer, *J. Geophys. Res.*, **106**, 33,463–33,469, doi:10.1029/2001JD001051.
- Chen, Y., F. Weng, Y. Han, and Q. Liu (2008), Validation of the Community Radiative Transfer Model by using CloudSat data, *J. Geophys. Res.*, **113**, D00A03, doi:10.1029/2007JD009561. [Printed 114(D8), 2009.]
- Chen, Y., Y. Han, P. Van Delst, and F. Weng (2010), On water vapor Jacobian in fast radiative transfer model, *J. Geophys. Res.*, **115**, D12303, doi:10.1029/2009JD013379.
- Chevallier, F., S. D. Michele, and A. P. McNally (2006), Diverse profile datasets from the ECMWF 91-level short-range forecast, *Rep. NWP SAF-EC-TR-010*, Satell. Appl. Facil. for Numer. Weather Predict, Exeter, U. K.
- Chin, M., R. B. Rood, S.-J. Lin, J.-F. Muller, and A. M. Thompson (2000), Atmospheric sulfur cycle simulated in the global model GOCART: Model description and global properties, *J. Geophys. Res.*, **105**, 24,671–24,687, doi:10.1029/2000JD900384.
- Christidis, N., M. D. Hurley, S. Pinnock, K. P. Shine, and T. J. Wallington (1997), Radiative forcing of climate change by CFC-11 and possible CFC replacements, *J. Geophys. Res.*, **102**, 19,597–19,609, doi:10.1029/97JD01137.
- Ciddor, P. E. (1996), Refractive index of air: New equations for the visible and near infrared, *Appl. Opt.*, **35**, 1566–1573, doi:10.1364/AO.35.001566.
- Clough, S. A., M. W. Shephard, E. J. Mlawer, J. S. Delamere, M. J. Iacono, K. Cady-Pereira, S. Boukabara, and P. D. Brown (2005), Atmospheric radiative transfer modeling: A summary of the AER codes, *J. Quant. Spectrosc. Radiat. Transfer*, **91**, 233–244, doi:10.1016/j.jqsrt.2004.05.058.
- Coheur, P. F., C. Clerbaux, and R. Colin (2003), Spectroscopic measurements of halocarbons and hydrohalocarbons by satellite-borne remote sensors, *J. Geophys. Res.*, **108**(D4), 4130, doi:10.1029/2002JD002649.
- Dufour, G., C. D. Boone, and P. F. Bernath (2005), First measurements of CFC-113 and HCFC-142b from space using ACE-FTS infrared spectra, *Geophys. Res. Lett.*, **32**, L15509, doi:10.1029/2005GL022422.
- Elkins, J. M., T. Thompson, T. Swanson, J. Butler, B. Hall, S. Cummings, D. Fisher, and A. Raffo (1993), Decrease in the growth rates of atmospheric chlorofluorocarbon-11 and chlorofluorocarbon-12, *Nature*, **364**, 780–783, doi:10.1038/364780a0.
- Han, Y., X. Xiong, P. van Delst, Y. Tahara, L. M. McMillin, and T. J. Kleespies (2003), An improved OPTRAN Algorithm, paper presented at Thirteenth International ATOVS Study Conference, Int. TOVS Working Group, Quebec, Que., Canada. [Available at http://cimss.ssec.wisc.edu/itwg/itsc/itsc13/proceedings/posters/b18_han.pdf.]
- Han, Y., P. van Delst, Q. Liu, F. Weng, B. Yan, R. Treadon, and J. Derber (2006), JCSDA Community Radiative Transfer Model (CRTM)—Version 1, *NOAA Tech. Rep. NESDIS 122*, 40 pp., NOAA, Camp Springs, Md.
- Heidinger, A. K. (2004), CLAVR-x Cloud Mask, algorithm theoretical basis document, NOAA, Camp Springs, Md.
- Ignatov, A., J. Sapper, I. Laszlo, N. Nalli, A. Harris, W. Pichel, A. E. Strong, E. Bayler, X. Li, and E. Maturi (2004), Global operational sea surface temperature and aerosol products from AVHRR: Current status, diagnostics, and potential enhancements, paper presented at 13th AMS Conference on Satellite Oceanography and Meteorology, Am. Meteorol. Soc., Norfolk, Va.
- Liang, X.-M., A. Ignatov, and Y. Kihai (2009), Implementation of the Community Radiative Transfer Model in Advanced Clear-Sky Processor for Oceans and validation against nighttime AVHRR radiances, *J. Geophys. Res.*, **114**, D06112, doi:10.1029/2008JD010960.
- Liu, Z., T. Auligne, H.-C. Lin, D. Bark, X. Zhang, and H. Shao (2008), Radiance data assimilation for WRF model: Overview and results, paper presented at Sixteenth International ATOVS Study Conference, Int. TOVS Working Group, Angra dos Reis, Brazil, 7–13 May.
- McClain, E. P., W. G. Pichel, and C. C. Walton (1985), Comparative performance of AVHRR-based multichannel sea surface temperatures, *J. Geophys. Res.*, **90**, 11,587–11,601, doi:10.1029/JC090iC06p11587.
- McMillin, L. M., X. Xiong, Y. Han, T. J. Kleespies, and P. Van Delst (2006), Atmospheric transmittance of an absorbing gas. 7. Further improvements to the OPTRAN 6 approach, *Appl. Opt.*, **45**, 2028–2034, doi:10.1364/AO.45.002028.
- Molina, M., and F. Rowland (1974), Stratospheric sink for chlorofluoromethanes: Chlorine atom-catalysed destruction of ozone, *Nature*, **249**, 810–812, doi:10.1038/249810a0.
- Nalli, N. R., P. J. Minnett, and P. van Delst (2008a), Emissivity and reflection model for calculating unpolarized isotropic water surface-leaving radiance in the infrared. 1: Theoretical development and calculations, *Appl. Opt.*, **47**, 3701–3721, doi:10.1364/AO.47.003701.
- Nalli, N. R., P. J. Minnett, E. Maddy, W. W. McMillan, and M. D. Goldberg (2008b), Emissivity and reflection model for calculating unpolarized isotropic water surface-leaving radiance in the infrared. 2: Validation using Fourier transform spectrometers, *Appl. Opt.*, **47**, 4649–4671, doi:10.1364/AO.47.004649.
- Reynolds, R. W., T. M. Smith, C. Liu, D. B. Chelton, K. S. Casey, and M. G. Schlax (2007), Daily high-resolution blended analyses for sea surface temperature, *J. Clim.*, **20**, 5473–5496, doi:10.1175/2007JCLI1824.1.
- Rienecker, M. M., et al. (2011), MERRA: NASA's Modern-Era Retrospective Analysis for Research and Applications, *J. Clim.*, **24**, 3624–3648, doi:10.1175/JCLI-D-11-00015.1.
- Rothman, L. S., et al. (2005), HITRAN 2004 molecular spectroscopic database, *J. Quant. Spectrosc. Radiat. Transfer*, **96**, 139–204, doi:10.1016/j.jqsrt.2004.10.008.
- Saunders, R. W., and D. P. Edwards (1989), Atmospheric transmittances for the AVHRR channels, *Appl. Opt.*, **28**, 4154–4160, doi:10.1364/AO.28.004154.
- Saunders, R. M., M. Matricardi, and P. Brunel (1999), An improved fast radiative transfer model for assimilation of satellite radiance observation, *Q. J. R. Meteorol. Soc.*, **125**, 1407–1425, doi:10.1256/smsqj.55614.
- Stark, J. D., C. J. Donlon, M. J. Martin, and M. E. McCulloch (2007), OSTIA: An operational, high resolution, real time, global sea surface temperature analysis system, in *OCEANS 2007 - Europe*, pp. 1–4, IEEE Press, Piscataway, N. J.
- Strow, L. L., S. E. Hannon, S. D. Souza-Machado, H. E. Mottler, and D. Tobin (2003), An overview of the AIRS radiative transfer model, *IEEE Trans. Geosci. Remote Sens.*, **41**, 303–313, doi:10.1109/TGRS.2002.808244.
- Taylor, P. C., and R. G. Ellingson (2008), A study of probability of clear line of sight through single-layer cumulus cloud fields in the tropical western pacific, *J. Atmos. Sci.*, **65**, 3497–3512, doi:10.1175/2008JAS2620.1.
- Walker, S. J., R. F. Weiss, and P. K. Salameh (2000), Reconstructed historic of the annual mean atmospheric mole fractions for halocarbons CFC-11, CFC-12, CFC-113, and carbon tetrachloride, *J. Geophys. Res.*, **105**, 14,285–14,296, doi:10.1029/1999JC900273.
- Weng, F., Y. Han, P. van Delst, Q. Liu, and B. Yan (2005), JCSDA community radiative transfer model (CRTM), paper presented at Fourteenth International ATOVS Study Conference, Int. TOVS Working Group, Beijing.
- World Meteorological Organization (WMO) (1988), The Montreal Protocol on substances that deplete the ozone layer, *WMO Bull.* **37**, pp. 94–97. Geneva, Switzerland.
- World Meteorological Organization (WMO) (2007), Scientific assessment of ozone depletion: 2006, *Global Ozone Res. Monit. Proj. Rep.* **50**, 572 pp, Geneva, Switzerland.
- Wu, X., and W. L. Smith (1997), Emissivity of rough sea surface for 8–13 μm : Modeling and verification, *Appl. Opt.*, **36**, 2609–2619, doi:10.1364/AO.36.002609.

Y. Chen, Joint Center for Satellite Data Assimilation, 5200 Auth Rd., Rm. 712, Camp Springs, MD 20746, USA.

Y. Han and F. Weng, Center for Satellite Applications and Research, National Environmental Satellite, Data, and Information Service, NOAA, 5200 Auth Rd., Rm. 712, Camp Springs, MD 20746, USA.